OXFORD

SOT | Society of Toxicology
academic.oup.com/toxsci

TOXICOLOGICAL SCIENCES, 182(1), 2021, 107–119

doi: 10.1093/toxsci/kfab042
Advance Access Publication Date: 21 April 2021
Research Article

Carbon Nanotube Exposure Triggers a Cerebral Peptidomic Response: Barrier Compromise, Neuroinflammation, and a Hyperexcited State

Ekaterina Mostovenko,* Samantha Saunders,* Pretal P. Muldoon,* Lindsey Bishop,† Matthew J. Campen,‡ Aaron Erdely,† and Andrew K. Ottens *,1

*Department of Anatomy and Neurobiology, Virginia Commonwealth University, Richmond, Virginia 23298, USA †Pathology and Physiology Research Branch, National Institute for Occupational Safety and Health, Morgantown, West Virginia 26505, USA and ‡Department of Pharmaceutical Sciences, University of New Mexico, Albuquerque, New Mexico 87131, USA

[1]To whom correspondence should be addressed at Department of Anatomy and Neurobiology, Virginia Commonwealth University, PO Box 980709, Richmond, VA 23298-0709. E-mail: akottens@vcu.edu.

ABSTRACT

The unique physicochemical properties of carbon nanomaterials and their ever-growing utilization generate a serious concern for occupational risk. Pulmonary exposure to these nanoparticles induces local and systemic inflammation, cardiovascular dysfunction, and even cognitive deficits. Although multiple routes of extrapulmonary toxicity have been proposed, the mechanism for and manner of neurologic effects remain minimally understood. Here, we examine the cerebral spinal fluid (CSF)-derived peptidomic fraction as a reflection of neuropathological alterations induced by pulmonary carbon nanomaterial exposure. Male C57BL/6 mice were exposed to 10 or 40 μg of multiwalled carbon nanotubes (MWCNT) by oropharyngeal aspiration. Serum and CSFs were collected 4 h post exposure. An enriched peptide fraction of both biofluids was analyzed using ion mobility-enabled data-independent mass spectrometry for label-free quantification. MWCNT exposure induced a prominent peptidomic response in the blood and CSF; however, correlation between fluids was limited. Instead, we determined that a MWCNT-induced peptidomic shift occurred specific to the CSF with 292 significant responses found that were not in serum. Identified MWCNT-responsive peptides depicted a mechanism involving aberrant fibrinolysis (fibrinopeptide A), blood-brain barrier permeation (homeobox protein A4), neuroinflammation (transmembrane protein 131L) with reactivity by astrocytes and microglia, and a pro-degradative (signal transducing adapter molecule, phosphoglycerate kinase), antiplastic (AF4/FMR2 family member 1, vacuolar protein sorting-associated protein 18) state with the excitation-inhibition balance shifted to a hyperexcited (microtubule-associated protein 1B) phenotype. Overall, the significant pathologic changes observed were consistent with early neurodegenerative disease and were diagnostically reflected in the CSF peptidome.

Key words: nanoparticles; carbon nanotubes; blood-brain barrier; neuroinflammation; peptidomics; peptidome; mass spectrometry; cerebrospinal fluid; excitotoxicity; neurodegenerative disease.

Nanoparticles, whether engineered or naturally occurring, represent a serious occupational and public health risk. Engineered nanomaterials such as multiwalled carbon nanotubes (MWCNT) have been shown to induce pulmonary fibrosis and tumor formation (Mercer *et al.*, 2013; Muller *et al.*, 2005; Porter *et al.*, 2010; Sargent *et al.*, 2014). Moreover, health outcomes of

Impact Statement

These studies demonstrate in a model of nanotube pulmonary exposure that there is a distinct CSF peptidomic response diagnostic of a compromised blood-brain barrier, neuroinflammation, and a hyperexcited neuronal state that is consistent with early pathobiology of neurodegenerative disease.

MWCNT pulmonary exposure have been detected far beyond the lung, despite limited translocation into the circulation and beyond (Mercer *et al.*, 2013): systemic inflammation (Erdely *et al.*, 2009), atherosclerosis (Niwa *et al.*, 2007), vascular dysfunction (Li *et al.*, 2007; Nurkiewicz *et al.*, 2006; Walker *et al.*, 2009), and even cognitive deficits (Liao *et al.*, 2014). Thus, extrapulmonary toxic burden of inhaled nanoparticles is of concern, with evidence for neurological impacts through as-yet unknown processes (Aragon *et al.*, 2017).

Translocation of the nanoparticles beyond the lung is recognized as a potential mediator of acute systemic toxicity (Deng *et al.*, 2007; Nemmar *et al.*, 2002; Reddy *et al.*, 2010); however, in a detailed study, Mercer *et al.* found that with MWCNT, just 0.01% of inhaled particulate mass reached peripheral organs and only 0.001% was evident within the brain (Mercer *et al.*, 2013). Alternatively, nanoparticle deposition deep within the alveolar space can induce immunologic and oxidative defense responses, leading to spillover of factors into the circulation (Donaldson *et al.*, 2005; Miller *et al.*, 2012). Yet several studies report on systemic health outcomes following carbon nanotube exposure without any sign of pulmonary inflammation (Khandoga *et al.*, 2010; Upadhyay *et al.*, 2008) or oxidative stress (Tabet *et al.*, 2009). Such findings prompted us and others to investigate alternative indirect molecular mediators of extrapulmonary outcomes (Erdely *et al.*, 2009; Mandler *et al.*, 2017, 2018; Mitchell *et al.*, 2009). Recently we reported the induction of bioactive peptides transferred between the lung and circulation after MWCNT pulmonary exposure in mice (Mostovenko *et al.*, 2019). Exemplifying this response, we identified a cleaved peptide from thrombospondin that significantly increased within the lung and circulation, synthesized it, and demonstrated its antiangiogenic capacity. Indeed, by isolating the sub 10 kDa peptide fraction from the serum of MWCNT-exposed animals, we were able to recapitulate much of the pro-inflammatory effects and vascular dysfunction produced by whole serum when placed on naïve cultured endothelial cells and vasculature. These findings helped establish the existence of a nanoparticle-induced peptidomic fraction as a contributing mediator of extrapulmonary outcomes.

In the same mouse model, we also found significant permeation of the blood-brain barrier (BBB) and proximal neuroinflammation after MWCNT exposure (Aragon *et al.*, 2017). Moreover, BBB dysfunction and neuroinflammation was abolished with prophylactic pretreatment with fasudil, a rho kinase inhibitor known to protect BBB integrity, which supported a causal relationship between barrier permeation and parenchymal perturbation. A compromised BBB "opens" the brain to exogenous molecular factors that can promote neuroinflammation and consequently alter neuronal function. Particulate-driven BBB disruption and neuroinflammation, including at the nanoscale, has been recognized for its probable pathogenic role in neurodegenerative disease (Block and Calderón-Garcidueñas, 2009; Gillespie *et al.*, 2013; Kleinman *et al.*, 2008; Schikowski *et al.*, 2015; Wang *et al.*, 2017). Building on our prior findings of MWCNT-exposure driven proteolytic products being released into the circulation and an opening of the BBB, we posited here that exposure-induced peptides enter the brain parenchyma where they may then drive glial and neuronal pathological outcomes. To test this hypothesis, we studied paired serum and cerebrospinal fluid (CSF) peptidomes for correlating shifts in response to MWCNT exposure as well as unique responses within the CSF peptidome. The diagnostic relevance of identified CSF peptides was then assessed in relation to cellular perturbation at the neurovascular unit and adjoining brain parenchyma.

MATERIALS AND METHODS

Animals, exposure, and sample collection. Specific pathogen-free male C57BL/6J mice (Jackson Laboratory, Bar Harbor, Maine) were used for this work. Animals were housed at the National Institute for Occupational Safety and Health in an Association for Assessment and Accreditation of Lab Animal Care International-approved animal facility. Animal care and use procedures were conducted in accordance with the U.S. Public Health Service's Policy on Humane Care and Use of Laboratory Animals and the National Institutes of Health's Guide for the Care and Use of Laboratory Animals. Mice were housed in ventilated cages in a temperature and humidity-controlled environment with a 12-h light/dark cycle, while food and tap water were available ad libitum. Eight-week-old mice received 0 μg ($n = 7$, control), 10 μg ($n = 6$), or 40 μg ($n = 6$) of MWCNT-7 (Hodogaya, Japan) nanotubes via oropharyngeal aspiration, with all animals receiving the vehicle dispersion media (0.6 mg/ml mouse serum albumin and 10 μg/ml 1,2-dipalmitoyl-sn-glycero-3-phosphocholine). This model was developed by the National Institute of Occupational Safety and Health to investigate the toxicological burden of a representative MWCNT at high occupationally relevant doses to explore outcomes in a compressed timeframe (Porter *et al.*, 2010). Moreover, the same model and MWCNT doses used here were consistent with our previous peptidomic work in serum and bronchoalveolar lavage fluid (Mostovenko *et al.*, 2019). The MWCNT-7 was characterized to have an average diameter and length of 49 nm and 3.86 μm (geometric SD = 1.94), respectively, was >99% pure carbon, and was lipopolysaccharide negative. Consistent with our past studies assessing circulating ligands and their role in promoting systemic pathology, biofluids, and tissues here were collected at 4 h post exposure (Aragon *et al.*, 2016, 2017; Erdely *et al.*, 2009; Mostovenko *et al.*, 2019). At 4 h, circulating factors were found to induce effects ex vivo that reflected systemic pathology; thus, this has been an ideal time to initially investigate early mediators. Animals were anesthetized under 2.5% isoflurane and immobilized within a stereotaxic frame. A 100 μl capacity pulled glass tip was inserted by micromanipulator into the cisterna magna and allowed to collect >20 μl of CSF for 20 min. Blood was then collected via cardiac puncture, allowed to clot, and centrifuged to collect serum. Animals were immediately decapitated after blood collection, brains removed, and snap frozen within 1 min. All materials were transferred to Virginia Commonwealth University on dry ice and stored at −80°C until use.

Endogenous peptide enrichment and mass spectral analysis. The peptidomic fraction from serum and CSF were generated as published previously (Mostovenko *et al.*, 2019). Briefly, 40 µl of serum and 20 µl of CSF were clarified through a 0.22 µm ultrafree MC filtration unit (EMDMillipore, Billerica, Massachusetts). The filtrate was denatured with 20% acetonitrile and reduced with 18 mM TCEP with HALT cocktail (Thermo Scientific, Rockford, Illinois) added for protease and phosphatase inhibition. Cysteine reduction was maintained with 30 mM iodoacetamide alkylation. MicroCon YM-30 (EMDMillipore) centrifugal filter units were used to resolve the peptide fraction (~8 kDa upper limit), with a second collection spin performed after acidification with 0.4% formic acid to further disrupt peptide binding. Crude peptide fractions were then loaded (4 µl for serum and 8 µl for CSF) onto a Symmetry C18 trap column (Waters, Milford, Massachusetts) to remove lipids, reagents and salts. Peptides were resolved by gradient reversed-phase chromatography between 6% and 44% acetonitrile in water (0.1% formic acid) over 65 min using a 150 mm × 75 µm HSS T3 column at 55°C, coupled online with a Synapt G2-Si tandem mass spectrometer (Waters). Data were acquired with ion mobility-enabled data-independent acquisition (UDMSe) between 400 and 1800 *m/z* at 25 000 nominal resolution (Distler *et al.*, 2016). Raw spectral data were processed as described previously (Mostovenko *et al.*, 2019) using PLGS v3.0.3 software (Waters) for peak picking, chromatographic peak area integration, and precursor-product ion alignment, and aligned across biological replicate were by retention time (±2 min), drift time (±5 bins), and ion mass (MH^+, ±12 ppm) in EndogeSeq. Data were then filtered to retain reproducible ion features (4+ replicate measures per group).

Immunofluorescent microscopy. The right hemisphere of each fresh-frozen mouse brain was cryosectioned (10 µm thick) along the sagittal plan starting 1 mm from midline. Sections were collected on charged slides, air dried, and then fixed with 4% paraformaldehyde. Sections were blocked and permeabilized in 5% normal goat serum and 0.1% Triton X-100 for 1 h at room temperature. Sections were then probed at 4°C overnight with primary antibodies in blocking buffer: vascular marker anti-rat ZO1 tight junction protein 1 (Developmental Studies Hybridoma Bank, Iowa City, Iowa; R26.4C, 1:5), BBB permeation marker anti-rabbit albumin (Bioss, bs-2256R, 1:300), microglial marker anti-guinea pig IBA1 (Synaptic Systems, Goettingen, Germany; 234-004, 1:2000), astrocytic marker anti-chicken GFAP (Abcam, Cambridge, Massachusetts; ab4674, 1:3000), glutamatergic synaptic marker anti-guinea pig Vglut1 (EMDMillipore, AB5905, 1:1000), and GABAergic synaptic marker anti-mouse Gad65 (Developmental Studies Hybridoma Bank, GAD-6, 1:5). Sections were then probed with corresponding AlexaFluor 488/568/680-conjugated goat secondary antibodies at room temperature for 2 h. Mounted sections were cover-slipped in ProLong Diamond Antifade Mountant (Thermo Scientific). Slides were imaged via multichannel immunofluorescence with a Zeiss AxioImager M2 microscope with structured illumination for both widefield and optical sectioning (0.25-µm stack thickness). Image acquisition and processing were performed with Zeiss Zen 2.1 software, with 12 images collected per brain region across 3 sections per animal, and region of interest quantitative analysis was performed in Fiji (Schindelin *et al.*, 2012). Images were centered on cerebrovasculature, as described previously (Aragon *et al.*, 2017), and a 100-µm diameter region of interest was then centered on the vessel for densitometry, with the vessel luminal area excluded. GFAP and IBA1 staining were then assessed for area fraction and mean fluorescence intensity within the region of interest with positive staining determined using the Otsu threshold algorithm, standardized across all sections for unbiased measurements.

Statistical and informatic analysis. Mass spectrometric peak area intensity data were median centered, imputed for left-censored data reproducibly falling below the limit of detection across at least 5 of 6 replicates per group, $\log_2$ transformed, and standardized to the average intensity across the 0 µg MWCNT control group, as described previously (Mostovenko *et al.*, 2019). An effect of MWCNT dose was assessed using 1-way ANOVA in MultiExperimentViewer (v.4.9.0), corrected for multiple peptide measures using the Benjamini-Hochberg false discovery rate method to control type 1 error to 5%. Pearson's correlation was used between serum and CSF peptidomic values in R, with results corrected for multiple measurements using Benjamini-Hochberg correction. Significant responsive peptide features were searched against targeted databases for matrix protease substrates and secretory proteins with results limited to a 5% false identification rate at the peptide level as published previously (Mostovenko *et al.*, 2019). Significantly responsive CSF peptides were aligned with corresponding serum features by retention time (±2 min), drift time (±5 bins), and ion mass (MH^+, ±12 ppm) to assess linear correlation in the measured peptide quantity across biofluids via the Pearson test in R studio (v1.1). Immunofluorescence microscopy measures were standardized to the average measure for the 0 µg MWCNT control group and assessed using 2-way ANOVA (MWCNT dose × brain region) with the Holm-Sidak multiple comparisons procedure for pairwise analysis within SigmaPlot (v14).

RESULTS

MWCNT Inhalation Exposure Promotes a Largely Independent CSF-Peptidomic Response

We recently published on the highly diverse peptidomic response to pulmonary MWCNT exposure across paired bronchoalveolar lavage fluid and serum (Mostovenko *et al.*, 2019). Here we assessed the peptidomic overlap between matched serum and CSF samples. Similar to our earlier study, we detected a diverse serum peptidome (6449 features) in this study, whereas in CSF, we measure 2226 reproducible features within the peptide-enriched fraction (Figure 1A). Unexpectedly, we found only 8% overlap between the CSF and serum peptidomes with 658 common features (Figure 1A), while there was a 45% overlap in peptide factors responsive between lung lavage and serum earlier (Mostovenko *et al.*, 2019). Between CSF and serum, just 4 of the 658 common factors (0.6%) exhibited significant within-animal correlation across all MWCNT doses (Figure 1B), which reflected almost no peptidomic cross-correlation between serum and CSF. These results were contrary to the present hypothesis, having posited that reported BBB dysfunction with this model (Aragon *et al.*, 2017) would have resulted in greater communication between serum and CSF.

In contrast to our expectation, 70% (1568) of the detected CSF factors were exclusively detected in CSF—not detected within serum replicates—pointing to the specificity of the CSF peptidome. ANOVA results indicated that 291 CSF-distinct peptide measures were significantly responsive to MWCNT exposure at a 5% FDR (Figure 2A), with 192 (66%) exhibiting a dose-independent response. Thus, while there was little crosstalk between the circulation and CSF, a neuropathological response to

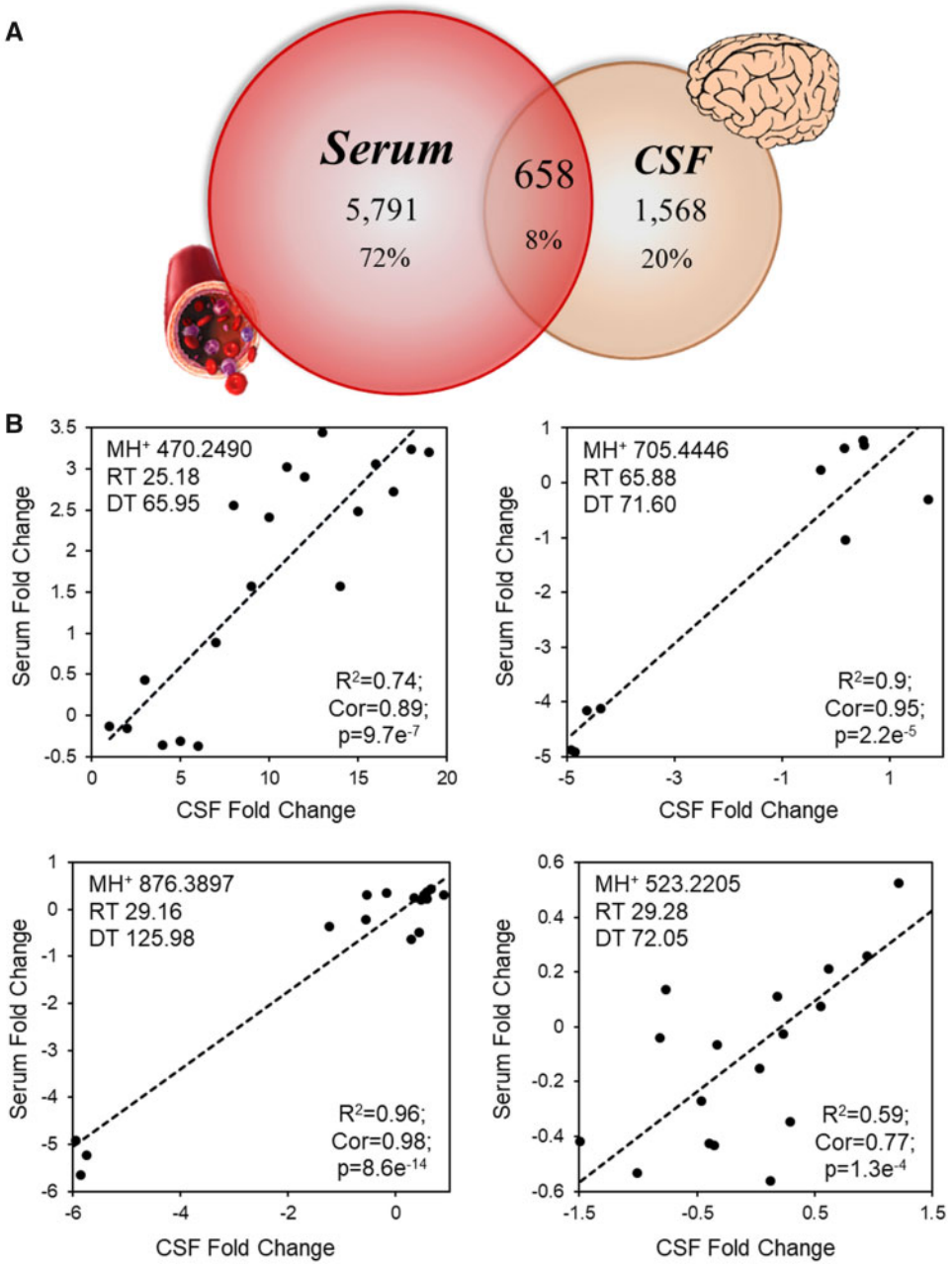

Figure 1. Limited correlation between serum and CSF peptidomic responses to pulmonary MWCNT exposure. Matched serum and CSF collected 4 h after MWCNT exposure was fractionated to enrich for endogenous peptides and analyzed by ion mobility-enabled data-independent mass spectrometry. A, Overlap in reproducibly ($n \geq 4$) detected peptide measures between serum and CSF, defined by a signature of common retention time (RT), ion mobility drift time (DT), and accurate mass measures (MH+). B, The log(2) relative ion intensity plotted across serum and CSF measures for the four peptides found with significant linear correlation. The square of the Pearson product-moment coefficient (R^2), Pearson's correlation coefficient (Cor), and p-values are noted, $n = 6$–7/group.

MWCNT exposure was evident by the significant influence on the CSF peptidome.

CSF-Specific Peptidomic Response Diagnostic of Neuroinflammation and Synaptic Plasticity

We employed the tandem mass spectral data collected across the MWCNT-responsive CSF peptidome to identify sequences and inform on functional relevance. We identified 8 unique endogenous peptides (Figure 2B) from a targeted matrix protease substrate database (Mostovenko *et al.*, 2019). As these were among those peptides exclusively detected within CSF, there was no overlap with our previously published MWCNT-responsive peptides identified in serum or lung lavage fluid (Mostovenko *et al.*, 2019). Peptides from AFF1 (AF4/FMR2 family member 1), HOXA4 (homeobox protein Hox-A4), and STAM (signal transducing adapter molecule 1) were affected in a dose-independent manner. The AFF1 peptide decreased 87.2-fold at 10 μg and 101-fold at 40 μg MWCNT. Similarly, the HOXA4 peptide was depleted 109-fold in both groups. In contrast, the STAM peptide significantly increased 231.8- and 115.6-fold, respectively, following 10 μg and 40 μg exposures. Peptides to fibrinogen alpha chain (FGA, decreased 48.3-fold), microtubule-associated protein 1B (MAP1B, decreased 100.3-fold), phosphoglycerate kinase 2 (PGK2, increased 117.8-fold), transmembrane

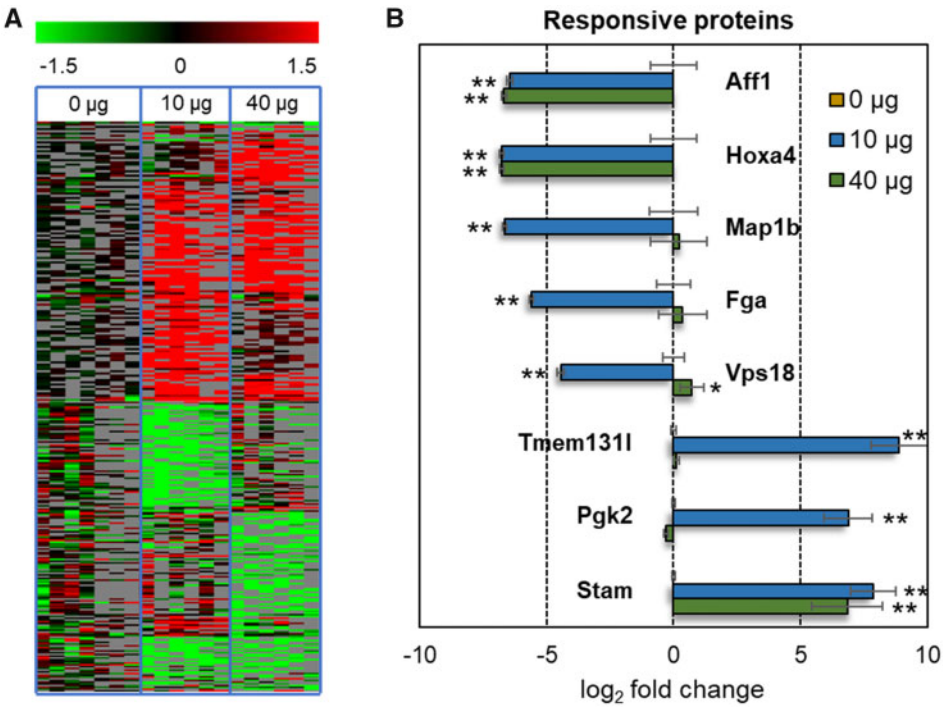

Figure 2. Significant CSF peptidomic response to pulmonary MWCNT exposure. CSF collected 4 h after MWCNT exposure was fractionated to enrich for endogenous peptides and analyzed by ion mobility-enabled data-independent mass spectrometry. A, Heat map representation of CSF peptide responses to 10 or 40 µg MWCNT exposures relative to the 0 µg control group. The log2 relative ion intensity is colored per the shown scale. B, The log(2) ion intensity relative to the 0 µg control group for identified peptides across 10 and 40 µg MWCNT exposures. Data are presented as mean ± SEM, $n = 6$–7/group. $^{*}p < .05$; $^{**}p < .001$.

protein 131-like (TMEM131L, increased 476.8-fold), and vacuolar protein sorting-associated protein 18 (Vps18, decreased 21.7-fold) were all significantly affected following the low dose exposure while exhibiting no change at 40 µg. This bifurcation between dose-independent and dose-dependent effects mirrored the overall CSF peptidomic response to MWCNT (Figure 2A).

Next, we assessed published roles for each originating protein within the brain. A full 75% of the identified peptides originate from proteins having distinct neurophysiological functions (Table 1). Functional annotations were assigned as proteins involved in: neuronal plasticity, AFF1, MAP1B, and Vps18 (Bouquet *et al.*, 2004; Kravtsov *et al.*, 2017; Peng *et al.*, 2012a; Tortosa *et al.*, 2011); neuronal survival, Vsp18, and AFF1 (Bitoun *et al.*, 2009; Peng *et al.*, 2012b); cell migration, Vsp18, and FGA; modulating endo-lysosomal machinery, STAM (Yamada *et al.*, 2001); and vascular remodeling, HOXA4 (Kimura *et al.*, 2020). Little is known about PGK2 and TMEM131L in the brain; however, their paralogs PGK1 and Tmem131 have been shown to be involved in neuronal stress resistance (Chen *et al.*, 2015), glutamatergic transmission (Schousboe *et al.*, 2011) and neuroinflammation (Mannini *et al.*, 2019; Rao *et al.*, 2015). Thus, these findings inform on the relevance of the CSF-peptidomic response to MWCNT exposure, highlighting a connection with neuroinflammation, neuronal stress/survival, adapted plasticity, and portending a broader neurological consequence of exposure than previously reported.

MWCNT-Induced Neuroinflammatory Glial Activation Is In-Part Regionally Dependent

In follow-up to the pro-inflammatory and cell stress/survival associated peptide factors, we evaluated glial reactivity proximal to permeated cerebrovasculature and assessed regional selectivity between cortex, striatum, and thalamus. In agreement with blood-brain barrier disruption reported earlier in this model (Aragon *et al.*, 2017), significant albumin leakage was detected in the brain parenchyma within 100 µm of the vessel lumen (green, Figure 3A). Albumin staining increased 183.4% with 10 µg ($p = .0035$) and 211.6% with 40 µg ($p = .0023$) MWCNT exposures (percentages from 0 µg vehicle control group). Concurrently, there was a robust increase in astrocytic GFAP staining proximal to the leaking vasculature (Figure 3A). Astrocyte processes appeared dilated, which was consistent with the increased the area fraction that was GFAP+: main effect of MWCNT treatment ($F = 20.85$, $p < .001$); 179% at 10 µg ($p < .001$) and 157% at 40 µg ($p < .001$) doses (Figure 3B). Additionally, GFAP mean fluorescence intensity also increased: main effect of MWCNT treatment ($F = 15.58$, $p < .001$); 240% at 10 µg ($p < .001$) and 173% at 40 µg ($p = .012$) doses (Figure 3C), with assessments consistent with reactive astrocytosis. Moreover, astrocyte processes were engorged with leaked albumin (yellow streaks within red-visualized processes, Figure 3A) indicating astrocyte scavenging of leaked material.

Next we assessed whether reactive astrocytosis was regionally selective; however, there wasn't a significant 2-way interaction between MWCNT exposure and brain regions ($F = 1.08$, $p = .3349$ for GFAP+ area fraction; $F = 0.641$, $p = .533$ for mean fluorescent intensity) (Figure 3B and 3C). The GFAP+ area fraction and fluorescence intensity were significantly elevated at the 10 µg dose similarly in all brain regions (though with a trend higher in striatum). GFAP+ measures were consistently lower at the 40 µg dose, reaching significance between doses for the GFAP fluorescence intensity measures ($p = .011$). Dose-dependent differences were further evident in reactive astrocyte packing around the vessel (Figure 3A). With the 40 µg dose, reactive astrocytes were densely accumulated up against the leaking vascular lumen. At the 10 µg dose, however, reactive

Table 1. CSF Peptides Identified From Those Significantly Responsive to MWCNT Exposure

Protein ID	Protein Symbol	Protein Name	Peptide Sequence	Fold Change (10, 40)	Function in CNS	References
O88573	AFF1	AF4/FMR2 family member 1	GNAKPGKPQVKSDR	−6.45 −6.67	Promotes dendritic remodeling	Kravtsov *et al.* (2017), Oren-Suissa *et al.* (2017)
E9PV24	FGA	Fibrinogen alpha chain (fibrinopeptide A)	EDKGEFLSEGGGVR	−5.6 0.4	Marker of neuroinflammation, initiates astrogliosis/glial scar formation. Cell migration guidance	Clark *et al.* (2018), Petersen *et al.* (2017), Pous *et al.* (2020), Schachtrup *et al.* (2010)
P06798	HOXA4	Homeobox protein Hox-A4	QSAPHLPA PNPHAARQP	−6.78 −6.77	Suppresses vascular remodeling	Kimura *et al.* (2020)
P14873	MAP1B	Microtubule-associated protein 1B	DTKMSISEGT VSDKSATP	−6.65 0.22	Affects axon branching, synaptic formation and maturation	Bodaleo *et al.* (2016), Bouquet *et al.* (2004), Palenzuela *et al.* (2017), Tortosa *et al.* (2011)
P09041	PGK2	Phosphoglycerate kinase 2	MDEVVKATSNGCV TIIGGGDTATC CAKWGTEDK	6.88 −0.3	Mediates stress resistance, synaptic neurotransmission, and early-onset of Parkinson's disease by attenuating ATP levels[a]	Chen *et al.* (2015), Schousboe *et al.* (2011)
P70297	STAM	Signal transducing adapter molecule 1	LDICDKVGQ SRTGPKD	7.86 6.85	Essential for neuronal cell survival in vivo	Yamada *et al.* (2001)
Q3U3D7	TMEM131L	Transmembrane protein 131-like	CQQLKSCSLGS DDALHLEMNII VAVENSSKQ	8.9 0.1	Neuro inflammation[b]	Mannini *et al.* (2019), Rao *et al.* (2015)
Q8R307	Vps18	Vacuolar protein sorting-associated protein 18 homolog	LYVLNEEGGPAPV	−4.44 0.73	Supports dendrite development of Purkinje cells, critical for neuron cell survival	Peng *et al.* (2012a,b)

[a]Function and references reported for PGK1 (paralog of PGK2).
[b]Function and references reported for Tmem131 (paralog of TMEM131L).

astrocytes appeared spread out over a wider area implicating less chemoattraction toward the leaking vessel.

IBA1-associated microglial/macrophage reactivity was also significantly affected near the leaking vessels (Figure 4A), with main effects of MWCNT exposure for IBA1+ area fraction ($F = 68.40$, $p < .001$) and mean fluorescent intensity ($F = 18.80$, $p < .001$). Moreover, with IBA1 there were significant 2-way effects across brain regions for area fraction ($F = 6.39$, $p = .004$) (Figure 4B) and mean fluorescent intensity ($F = 4.58$, $p = .017$) (Figure 4C). The effect of MWCNT exposure on IBA1+ area fraction was greatest in striatum at both 10 μg (vs thalamus $p = .019$ and cortex $p = .017$) and 40 μg (vs thalamus $p = .006$ and cortex $p = .008$) doses, though the magnitude of effect was consistent between doses in all brain regions. For GFAP+ mean fluorescence intensity, there was again a greater effect in striatum over other brain regions, reaching significance at the 40 μg dose (vs thalamus $p = .007$ and cortex $p = .01$). There was also a significant dose dependency within striatum ($p = .019$), with intensity increasing 323% at 10 μg and 498% at 40 μg. As observed with astrocytes, reactive microglia appeared more spread out from the leaking vessel at the 10 μg dose relative to the 40 μg of MWCNT (Figure 4A). Together, these results indicate significant microglial/macrophage neuroinflammatory reactivity across all brain regions, with greater susceptibility in striatum, and greater chemoattraction toward the leaking vessel in the higher 40 μg dose.

MWCNT-Induced Excitatory/Inhibitory Synaptic Imbalance Proximal to Leaking Cerebrovasculature

The CSF peptidomic response further suggested altered synaptic plasticity after MWCNT exposure. To test this possibility, we assessed MWCNT-induced shifts in glutamatergic and GABAergic synaptic density using the selective markers Vglut1 and Gad65, respectively (Figure 5). Adjacent to the cerebrovasculature (within 100 μm), there was a significant main effect of MWCNT exposure ($F = 31.35$, $p < .001$) on Vglut1+ glutamatergic synaptic staining, which increased at both doses in all three brain regions from the 0 μg MWCNT control group (Figure 5A). A trend in the MWCNT effect on Vglut1+ staining was observed between regions: cortex (197%/183%; 10 μg/40 μg as % of 0 μg control) > striatum (180%/149%) > thalamus (151%/139%); however, this difference did not reach significance ($F = 2.27$, $p = .115$).

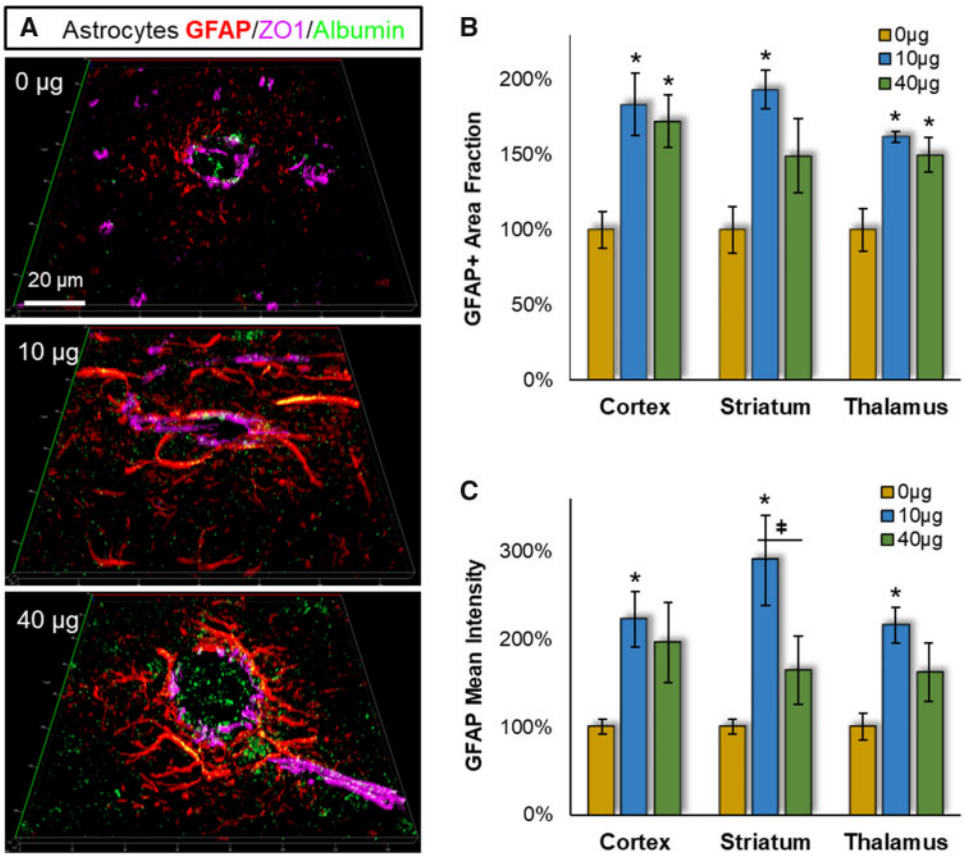

Figure 3. Pulmonary MWCNT exposure increased astrocyte reactivity across multiple brain regions. Brain tissues collected 4 h after exposure were stained with the astrocyte marker GFAP (red), the BBB permeation marker albumin (green), and the cerebrovasculature marker ZO1 (magenta). A, Representative GFAP staining proximal to cerebrovasculature are shown from striatum. B, The percent area within 100 µm of the ZO1 defined vessel wall was assessed across neocortex, striatum and thalamus, relative to the 0 µg control exposure group. C, The fluorescent intensity of GFAP staining within 100 µm of the vessel wall was assessed relative to the 0 µg control exposure group within neocortex, striatum, and thalamus. Data are presented as mean ± SEM, $n = 6$/group. *$p < .05$ within dose relative to 0 µg control; #$p < .05$ across brain regions;+$p < .05$ between doses within a brain region. Scale bar = 20 µm.

In contrast, significant main effects for MWCNT exposure ($F = 37.28$, $p < .001$) and brain region ($F = 7.03$, $p = .002$) were found for GABAergic inhibitory synaptic staining (Figure 5B). Post-hoc analysis showed that the response in cortex was significant different from striatum ($p = .005$) and thalamus ($p = .007$). Importantly, MWCNT exposure produced a prominent decrease in GABAergic staining (opposite to Vglut1 increase), with a greater effect at 10 µg over 40 µg ($p = .002$): cortex (32%/58%; 10 µg/40 µg as % of 0 µg control) > striatum (42%/75%) approximately thalamus (66%/66%). Morphologically, GABAergic staining appeared decreased throughout the area 100 µm from the vessel wall in both doses, reflecting a widespread response. This was different from the Vglut1 staining, where the MWCNT effect appeared more prominent closer up to the vessel lumen (Figure 4C). Taken together, increased Vglut1 and decreased Gad65 indicated a pronounced elevation in the excitatory/inhibitory (E/I) balance with MWCNT exposure, which appeared more pronounced in the cortex > striatum > thalamus. Notably, E/I imbalance is widely noted in the pathogenesis of neurodegenerative diseases (Davidkova and Carroll, 2007; García-Cabrero *et al.*, 2013; Palenzuela *et al.*, 2017; Selkoe, 2019; Shimojo *et al.*, 2020).

DISCUSSION

In this study, we revealed a substantive CSF-specific peptidomic response to MWCNT exposure. A majority 70% of peptides (1568) were detected only in CSF (no corresponding measure in serum). The remaining 30% of peptides (658) detected in both serum and CSF showed almost no evidence of molecular exchange in response to MWCNT exposure, with just 4 peptides (0.006%) showing significant correlation. Together, these data demonstrate negligible exchange between these biofluids in response to MWCNT exposure, despite prior evidence of an open BBB after nanoparticle exposure (Aragon *et al.*, 2017; Chen *et al.*, 2008; Hartz *et al.*, 2008; Oppenheim *et al.*, 2013). Explaining this, the BBB and blood-CSF barriers are physiologically distinct, with the later focused within the choroid plexus (Pardridge, 2016). With the BBB, tight junctions are between cerebrovascular endothelial cells, whereas the blood-CSF barrier is mediated through epithelial tight junctions. The choroid epithelium appears to remain intact with limit peptide communication into the CSF. Furthermore, efflux of peptide waste from brain tissue is theorized to occur via the glymphatic system, where CSF flows unidirectionally from the ventricles down along penetrating arterioles and between astrocytic end-feet into the parenchyma (Iliff *et al.*, 2012; Iliff and Nedergaard, 2013). This implies that peptide clearance across a leaking BBB goes from the interstitial fluid into perivenous channels and the cervical lymphatic system, further explaining how peptides leaked from the circulation are unlikely to reach a sufficient concentration within the CSF to be detected in our studies.

Yet, the CSF peptidome was clearly impacted after MWCNT exposure, with 291 peptides (18.6%) significantly altered. These

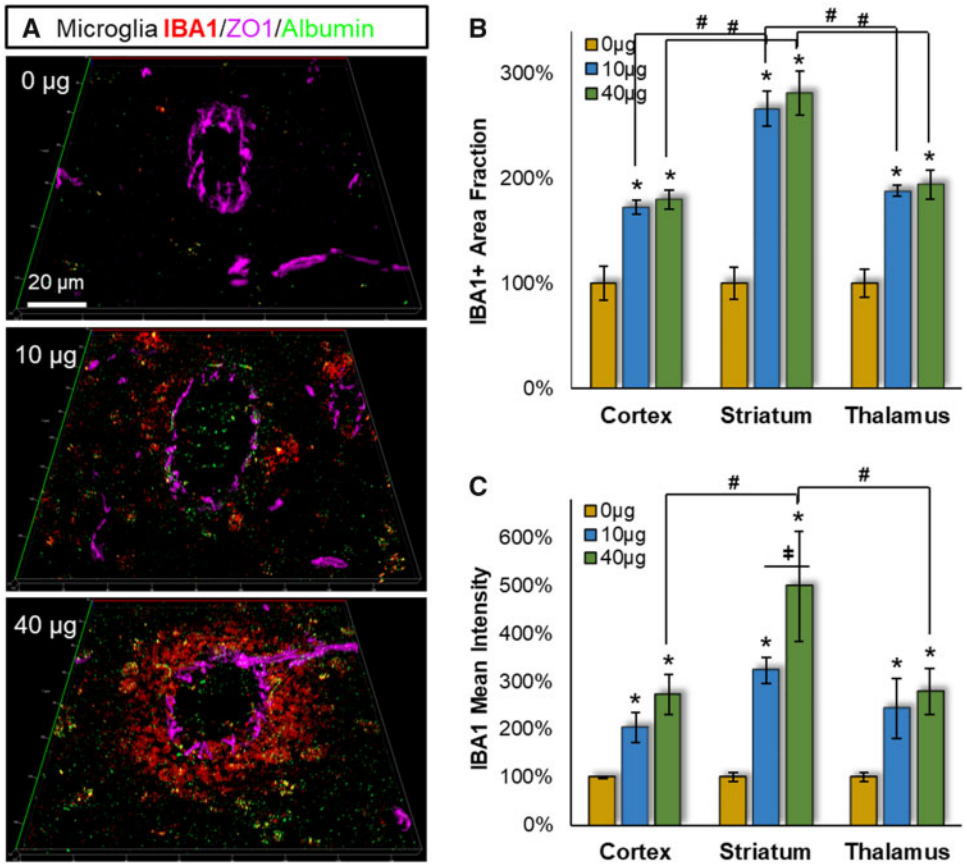

Figure 4. Pulmonary MWCNT exposure increased microglial reactivity across multiple brain regions. Brain tissues collected 4 h after exposure were stained with the microglial/macrophage marker IBA1 (red), the BBB permeation marker albumin (green), and the cerebrovasculature marker ZO1 (magenta). A, Representative IBA1 staining proximal to cerebrovasculature are shown from striatum. B, The percent area within 100 µm of the ZO1 defined vessel wall was assessed across neocortex, striatum, and thalamus, relative to the 0 µg control exposure group. C, The fluorescent intensity of IBA1 staining within 100 µm of the vessel wall was assessed relative to the 0 µg control exposure group within neocortex, striatum, and thalamus. Data are presented as mean ± SEM, $n = 6$/group. $^{*}p < .05$ within dose relative to 0 µg control; $\#p < .05$ across brain regions; $\mp, p < .05$ between doses within a brain region. Scale bar = 20 µm.

peptide effects were unique to CSF, with no corresponding detections in serum. Thus, we were particularly interested in gaining further insight into their pathobiological relevance. Recognizing that identification of endogenous peptides using tandem mass spectral data remains challenged by an unrestricted sequence-search space (Mostovenko *et al.*, 2019), we took measures to control false detections to only 5%, and successfully identified eight MWCNT-responsive peptides (Table 1) as a window into the neurobiological response.

Several peptides were derived from proteins indicative of vascular deficits and neuroinflammation. At both doses of MWCNT, HOXA4 significantly decreased, which is known to exacerbated vascular remodeling within the brain and other tissues (Kimura *et al.*, 2020). Also decreased, though only at the 10 µg dose, was a fibrinopeptide A fragment (residues 22–36) of FGA, indicating reduced fibrinolysis consistent with increased neurovascular damage and astrogliosis (Clark *et al.*, 2018; Pous *et al.*, 2020; Schachtrup *et al.*, 2010) as seen under neurodegenerative conditions (Paul *et al.*, 2007). Complementing this dose-dependent response was a 10-µg dose-selective increase in a peptide (residues 242–273) derived from the Wnt-inhibitory motif of TMEM131L (Maharzi *et al.*, 2013). TMEM131 proteins containing this motif (Zhang *et al.*, 2020) inhibits Wnt/β-catenin signaling via lysosome-dependent degradation of Wnt co-receptor LRP6 (Maharzi *et al.*, 2013). The Wnt/β-catenin pathway, in turn has broad effects on neuroinflammation, the BBB, and synaptic effects (Halleskog *et al.*, 2011; Liu *et al.*, 2014a,b). Together, these peptides offer a diagnostic view on dose-independent barrier compromise but with dose-dependent differences in glial reactivity and potentially downstream synaptic changes. Importantly, these results were affirmed via microscopy findings across several key structures (cortex, striatum, and thalamus) tied with mild cognitive impairment and Alzheimer's disease (Yi *et al.*, 2016). In familial Alzheimer's disease, the striatum and its target the thalamus are compromised early during pre-symptomatic pathogenesis (Ryan *et al.*, 2013), adding to the importance of evidence of preferential vulnerability in these regions.

Fibrinolysis dynamics in connection with BBB disruption is also associated with astrocytic and microglial reactivity found in the progression of Alzheimer's disease (Festoff *et al.*, 2016). Our results show pronounced glial reactivity proximal to leaking cerebrovasculature across all assessed brain regions, but striatum appeared particularly impacted. The glial reactivity found here was consistent with our previous report of elevated pro-inflammatory cytokines IL6 (reinforces a pro-inflammatory state) and CCL5 (recruits microglial migration) that indicated an M1 phenotypic response in MWCNT exposed animals (Aragon *et al.*, 2017). Previously we found that this neuroinflammation could be diminished by reinforcing BBB integrity with fasudil, supporting a causal relationship. Here we showed that with an increase in MWCNT dose, reactive glia more rapidly aggregate

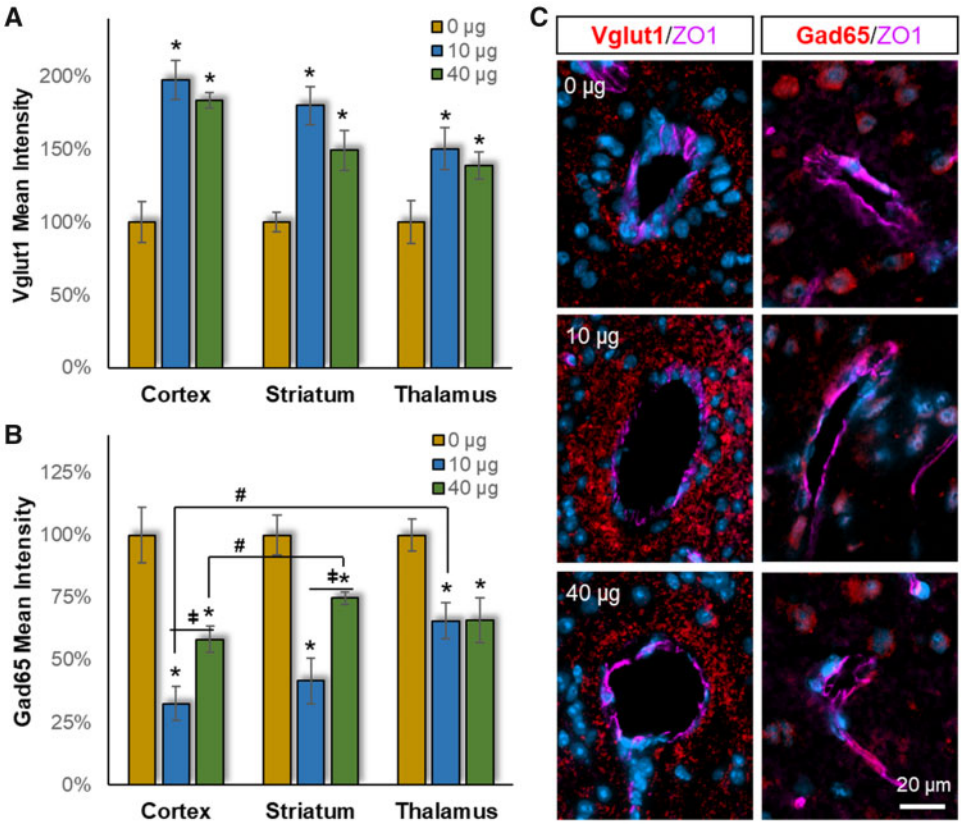

Figure 5. Pulmonary MWCNT exposure resulted in excitatory/inhibitory network imbalance. Brain tissues collected 4 h after exposure were stained with either the excitatory synaptic marker Vglut1 or the inhibitory synaptic marker Gad65 (red), with counter DAPI staining for nuclei (blue) and ZO1 staining for cerebrovasculature (magenta). Densitometric analysis of (A) Vglut1 or (B) Gad65 fluorescent intensity within 100 µm of the vessel wall was assessed relative to the 0 µg control exposure group within neocortex, striatum, and thalamus. (C) Representative Vglut1 and Gad65 staining proximal to cerebrovasculature are shown from striatum. Data are presented as mean ± SEM, $n = 6$/group. $^{*}p < .05$ within dose relative to 0 µg control; $\#p < .05$ across brain regions; $\ddagger p < .05$ between doses within a brain region. Scale bar = 20 µm.

around the leaking vessel consistent with glial scar initiation (Kawano *et al.*, 2012). Such processes involve proteolytic processing, a feature of progressive neurodegeneration (Dehay *et al.*, 2013; Malik *et al.*, 2019; Whyte *et al.*, 2017).

Evidence of early neurodegenerative processes was supported by the CSF peptidomic response to MWCNT. Decreased Vps18, indicated by a corresponding peptide, has been found to arrest dendritic outgrowth (Peng *et al.*, 2012a) and to precede neuronal cell death (Peng *et al.*, 2012b). Also decreased was an AFF1 peptide, which further supported a pro-degradative phenotype as this protein is essential to enabling plasticity after injury, and is consider a potential therapeutic target (Kravtsov *et al.*, 2017; Oren-Suissa *et al.*, 2017). Moving opposite in direction, the identified STAM peptide increased in concentration, a protein who's overexpression causes excessive ubiquitination and endosomal compartmentation (Mizuno *et al.*, 2003). These processes are yet another feature of neurodegenerative disease pathogenesis (Nixon, 2005). Lastly, increased levels of PGK also suggests neuronal stress (Chen *et al.*, 2015) and enhanced excitatory neurotransmission (Schousboe *et al.*, 2011). Thus, the CSF peptidomic response to MWCNT implies that beyond BBB disruption and observed glial reactivity there are likely changes to the neuronal circuitry that could impart longer-term consequences consistent with neurodegenerative pathogenesis.

Elevated excitation is yet another feature of early neurodegenerative disease (Vico Varela *et al.*, 2019) and other neurological disorders (Jia *et al.*, 2015). Hyperexcitability is associated with amyloid and tau pathology even before neurodegeneration begins in, for example, models of Alzheimer's disease and frontotemporal dementia (García-Cabrero *et al.*, 2013; Selkoe, 2019). Proteinopathy-related hyperexcitability occurs from an imbalance in excitation and inhibition (E/I) with concomitant reduce inhibitory transmission (Shimojo *et al.*, 2020). Co-staining with markers of excitatory and inhibitory synapses showed such an E/I imbalance, with significant elevations in Vglut1+ glutamatergic synapses and significantly diminished GAD65+ GABAergic synapses. An E/I imbalance was found in all examined brain regions, though more so in cortex. Interestingly, E/I imbalance in striatum and cortex was significantly worse in the 10 µg treated mice. Anatomically, increased excitatory staining was evident farther from the vascular lumen with the 10 µg dose than the 40 µg, suggesting a wider area of impacted synaptic function. This was consistent with micrographic observation of reactive glia found farther out from the leaking vessel in the 10 µg, whereas glial at the 40 µg dose were found densely aggregated around the vessel lumen as characteristic of glial scar initiation (Kawano *et al.*, 2012). Formation of a glial scar not only serves to confine and repair the disrupted BBB, but to also protect adjoining neuropil, suggesting that a more pronounced neuroinflammatory effect at the higher 40 µg dose may have helped abbreviate detrimental effects to neural circuitry. These findings were moreover consistent with significant dose-dependent peptide changes observed at the lower dose for Tmem131l, Vps18, and PGK peptides, which we've previously discussed for their relevance to synaptic effects. A further diagnostic link between the CSF peptidomic response and aberrant

synaptic plasticity was found with the dose-dependent decrease in the MAP1B peptide. MAP1B provides for dynamic internalization of glutamatergic receptors based on neurotransmission activity (Davidkova and Carroll, 2007; Palenzuela *et al.*, 2017). The decreased MAP1B peptide thus is indicative of more glutamatergic receptor available, another symptom of a hyperexcited state. MAP1B has been found depleted though binding with amyloid-beta (Gevorkian *et al.*, 2008) and promotes seizure susceptibility (Vico Varela *et al.*, 2019) in human Alzheimer's disease. Moreover, overexpression of MAP1B in an Alzheimer's model mouse was found to reverse cognitive decline (Mitsuyama and Koide, 2018). Altogether, results here portend E/I imbalance after MWCNT exposure, predisposing the brain to neuronal stress and degeneration in the longer term. E/I imbalance proximal to an impaired BBB is also suggestion of acute neurologic effects such as migraine (Vecchia and Pietrobon, 2012), which could be considered in future epidemiology on CNT workers. Importantly, E/I imbalance was greater at the lower 10 μg MWCNT exposure, with associated dose-dependent peptide responses in CSF. Thus, future studies are needed to interrogate whether lower, occupationally typical MWCNT exposures, produce such neuronal impacts.

In summary, this study revealed that although the BBB was compromise by MWCNT, peptides induced into the serum after exposure were largely absent from the CSF. However, the MWCNT insult induced a separate, yet sizable, shift within the CSF peptidome that was diagnostically informative of the glial reactivity and neuronal network E/I imbalance found proximal to leaking cerebrovasculature. To this end, the CSF peptidome provided a live-animal window on nanoparticle neurotoxicology that may also be useful with other xenobiotic exposures. Important in considering these initial results, only a single time point was investigated, limiting cause-effect determinations between the CSF peptidome and neuropathological outcomes. Further studies are needed to assess causation through CSF peptidomic bioactivity. Of further consideration, the MWCNT-7 material used here was surrogate for high-aspect nanomaterials, of which there is a growing diversity. We would expect similar neuropathology from other high-aspect materials with long latencies in the lung, but other nanomaterials that can be readily cleared through solubilization, phagocytosis, or even transcytosis may produce alternative findings. Additionally, modeled here was an acute response to a large amount of MWCNT, with the 10 μg dose approximates the amount of nanotube exposure a worker would experience over a month in a facility with a high 400 $\mu g/m^3$ ambient concentration (Porter *et al.*, 2010). These are extreme conditions relative to U.S. facilities, a dose that was selected to provide initial insight into potential pathobiology within a reasonable modeling observation period. Findings here are thus justification for further investigation into neurological consequences associated with repeated exposure at more typical MWCNT concentrations (10.6 $\mu g/m^3$ being the average across 8 U.S. facilities) over a protracted period (Erdely *et al.*, 2013). In all, the CSF peptidomic response to MWCNT exposure provided insight into ongoing neuropathological change within the brain that are phenotypically similar to early progression in neurodegenerative diseases such as Alzheimer's. Further studies are needed to explore the longer-term circuit and degenerative implications of engineered nanoparticle exposures.

ACKNOWLEDGMENTS

We thank Ambrine Chacko for assistance with immunofluorescent staining of brain tissues. The antibodies to ZO1 (R26.4C) and Gad65 (GAD-6) were developed by D.A. Goodenough at Harvard Medical School and D.I. Gottlieb at Washington University School of Medicine, respectively, and were obtained from the Developmental Studies Hybridoma Bank, created by the Eunice Kennedy Shriver National Institute of Child Health and Human Development (NICHD) and maintained at the University of Iowa. The findings and conclusions in this report are those of the authors and do not necessarily represent the official position of the National Institute for Occupational Safety and Health of the Centers for Disease Control and Prevention.

FUNDING

National Institute for Occupational Safety and Health (R01OH010495 to A.K.O. and M.J.C., NTRC 939ZXFL to A.E.).

DECLARATION OF CONFLICTING INTERESTS

The authors declare no conflicts of interest with respect to the research, authorship and/or publication of this article.

REFERENCES

Aragon, M., Erdely, A., Bishop, L., Salmen, R., Weaver, J., Liu, J., Hall, P., Eye, T., Kodali, V., Zeidler-Erdely, P., *et al.* (2016). MMP-9-dependent serum-borne bioactivity caused by multiwalled carbon nanotube exposure induces vascular dysfunction via the CD36 scavenger receptor. *Toxicol. Sci.* **150**, 488–498.

Aragon, M. J., Topper, L., Tyler, C. R., Sanchez, B., Zychowski, K., Young, T., Herbert, G., Hall, P., Erdely, A., Eye, T., *et al.* (2017). Serum-borne bioactivity caused by pulmonary multiwalled carbon nanotubes induces neuroinflammation via blood-brain barrier impairment. *Proc. Natl. Acad. Sci. U.S.A.* **114**, E1968–E1976.

Bitoun, E., Finelli, M. J., Oliver, P. L., Lee, S., and Davies, D. K. E. (2009). AF4 is a critical regulator of the IGF-1 signaling pathway during Purkinje cell development. *J. Neurosci.* **29**, 15366–15374.

Block, M. L., and Calderón-Garcidueñas, L. (2009). Air pollution: Mechanisms of neuroinflammation and CNS disease. *Trends Neurosci.* **32**, 506–516.

Bodaleo, F. J., Montenegro-Venegas, C., Henríquez, D. R., Court, F. A., and Gonzalez-Billault, C. (2016). Microtubule-associated protein 1B (MAP1B)-deficient neurons show structural presynaptic deficiencies in vitro and altered presynaptic physiology. *Sci. Rep.* **6**, 30069.

Bouquet, C., Soares, S., Von Boxberg, Y., Ravaille-Veron, M., Propst, F., and Nothias, F. (2004). Microtubule-associate protein 1B controls directionality of growth cone migration and axonal branching in regeneration of adult dorsal root ganglia neurons. *J. Neurosci.* **24**, 7204–7213.

Chen, L., Yokel, R. A., Hennig, B., and Toborek, M. (2008). Manufactured aluminum oxide nanoparticles decrease expression of tight junction proteins in brain vasculature. *J. Neuroimmune Pharmacol.* **3**, 286–295.

Chen, X., Zhao, C., Li, X., Wang, T., Li, Y., Cao, C., Ding, Y., Dong, M., Finci, L., Wang, J. H., *et al.* (2015). Terazosin activates Pgk1 and Hsp90 to promote stress resistance. *Nat. Chem. Biol.* **11**, 19–25.

Clark, V. D., Layson, A., Charkviani, M., Muradashvili, N., and Lominadze, D. (2018). Hyperfibrinogenemia-mediated astrocyte activation. *Brain Res.* **1699**, 158–165.

Davidkova, G., and Carroll, R. C. (2007). Characterization of the role of microtubule-associated protein 1B in metabotropic glutamate receptor-mediated endocytosis of AMPA receptors in hippocampus. *J. Neurosci.* **27**, 13273–13278.

Dehay, B., Martinez-Vicente, M., Caldwell, G. A., Caldwell, K. A., Yue, Z., Cookson, M. R., Klein, C., Vila, M., and Bezard, E. (2013). Lysosomal impairment in Parkinson's disease. *Mov. Disord.* **28**, 725–732.

Deng, X., Jia, G., Wang, H., Sun, H., Wang, X., Yang, S., Wang, T., and Liu, Y. (2007). Translocation and fate of multi-walled carbon nanotubes in vivo. *Carbon* **45**, 1419–1424.

Distler, U., Kuharev, J., Navarro, P., and Tenzer, S. (2016). Label-free quantification in ion mobility-enhanced data-independent acquisition proteomics. *Nat. Protoc.* **11**, 795–812.

Donaldson, K., Tran, L., Jimenez, L. A., Duffin, R., Newby, D. E., Mills, N., MacNee, W., and Stone, V. (2005). Combustion-derived nanoparticles: A review of their toxicology following inhalation exposure. *Part. Fibre Toxicol.* **2**, 10.

Erdely, A., Dahm, M., Chen, B. T., Zeidler-Erdely, P. C., Fernback, J. E., Birch, M. E., Evans, D. E., Kashon, M. L., Deddens, J. A., Hulderman, T., *et al.* (2013). Carbon nanotube dosimetry: From workplace exposure assessment to inhalation toxicology. *Part. Fibre Toxicol.* **10**, 53.

Erdely, A., Hulderman, T., Salmen, R., Liston, A., Zeidler-Erdely, P. C., Schwegler-Berry, D., Castranova, V., Koyama, S., Kim, Y. A., Endo, M., *et al.* (2009). Cross-talk between lung and systemic circulation during carbon nanotube respiratory exposure. Potential biomarkers. *Nano Lett.* **9**, 36–43.

Festoff, B. W., Sajja, R. K., van Dreden, P., and Cucullo, L. (2016). HMGB1 and thrombin mediate the blood-brain barrier dysfunction acting as biomarkers of neuroinflammation and progression to neurodegeneration in Alzheimer's disease. *J. Neuroinflammation* **13**, 194.

García-Cabrero, A. M., Guerrero-López, R., Giráldez, B. G., Llorens-Martín, M., Ávila, J., Serratosa, J. M., and Sánchez, M. P. (2013). Hyperexcitability and epileptic seizures in a model of frontotemporal dementia. *Neurobiol. Dis.* **58**, 200–208.

Gevorkian, G., Gonzalez-Noriega, A., Acero, G., Ordoñez, J., Michalak, C., Munguia, M. E., Govezensky, T., Cribbs, D. H., and Manoutcharian, K. (2008). Amyloid-β peptide binds to microtubule-associated protein 1B (MAP1B). *Neurochem. Int.* **52**, 1030–1036.

Gillespie, P., Tajuba, J., Lippmann, M., Chen, L. C., and Veronesi, B. (2013). Particulate matter neurotoxicity in culture is size-dependent. *Neurotoxicology* **36**, 112–117.

Halleskog, C., Mulder, J., Dahlström, J., Mackie, K., Hortobágyi, T., Tanila, H., Kumar Puli, L., Färber, K., Harkany, T., and Schulte, G. (2011). WNT signaling in activated microglia is proinflammatory. *Glia* **59**, 119–131.

Hartz, A. M. S. S., Bauer, B., Block, M. L., Hong, J.-S. S., and Miller, D. S. (2008). Diesel exhaust particles induce oxidative stress, proinflammatory signaling, and P-glycoprotein up-regulation at the blood-brain barrier. *Faseb J.* **22**, 2723–2733.

Iliff, J. J., and Nedergaard, M. (2013). Is there a cerebral lymphatic system? *Stroke* **44**, S93–S95.

Iliff, J. J., Wang, M., Liao, Y., Plogg, B. A., Peng, W., Gundersen, G. A., Benveniste, H., Vates, G. E., Deane, R., Goldman, S. A., *et al.* (2012). A paravascular pathway facilitates CSF flow through the brain parenchyma and the clearance of interstitial solutes, including amyloid β. *Sci. Transl. Med.* **4**, 147ra111.

Jia, M., Njapo, S. A. N., Rastogi, V., and Hedna, V. S. (2015). Taming glutamate excitotoxicity: Strategic pathway modulation for neuroprotection. *CNS Drugs* **29**, 153–162.

Kawano, H., Kimura-Kuroda, J., Komuta, Y., Yoshioka, N., Li, H. P., Kawamura, K., Li, Y., and Raisman, G. (2012). Role of the lesion scar in the response to damage and repair of the central nervous system. *Cell Tissue Res.* **349**, 169–180.

Khandoga, A., Stoeger, T., Khandoga, A. G., Bihari, P., Karg, E., Ettehadieh, D., Lakatos, S., Fent, J., Schulz, H., and Krombach, F. (2010). Platelet adhesion and fibrinogen deposition in murine microvessels upon inhalation of nanosized carbon particles. *J. Thromb. Haemost.* **8**, 1632–1640.

Kimura, M., Horie, T., Baba, O., Ide, Y., Tsuji, S., Ruiz Rodriguez, R., Watanabe, T., Yamasaki, T., Otani, C., Xu, S., *et al.* (2020). Homeobox A4 suppresses vascular remodeling by repressing YAP/TEAD transcriptional activity. *EMBO Rep.* **21**, e48389.

Kleinman, M. T., Araujo, J. A., Nel, A., Sioutas, C., Campbell, A., Cong, P. Q., Li, H., and Bondy, S. C. (2008). Inhaled ultrafine particulate matter affects CNS inflammatory processes and may act via MAP kinase signaling pathways. *Toxicol. Lett.* **178**, 127–130.

Kravtsov, V., Oren-Suissa, M., and Podbilewicz, B. (2017). The fusogen AFF-1 can rejuvenate the regenerative potential of adult dendritic trees by self-fusion. *Development* **144**, 2364–2374.

Li, Z., Hulderman, T., Salmen, R., Chapman, R., Leonard, S. S., Young, S. H., Shvedova, A., Luster, M. I., and Simeonova, P. P. (2007). Cardiovascular effects of pulmonary exposure to single-wall carbon nanotubes. *Environ. Health Perspect.* **115**, 377–382.

Liao, H. Y., Chung, Y. T., Lai, C. H., Wang, S. L., Chiang, H. C., Li, L. A., Tsou, T. C., Li, W. F., Lee, H. L., Wu, W. T., *et al.* (2014). Six-month follow-up study of health markers of nanomaterials among workers handling engineered nanomaterials. *Nanotoxicology* **8**(Suppl 1), 100–110.

Liu, C. C., Tsai, C. W., Deak, F., Rogers, J., Penuliar, M., Sung, Y. M., Maher, J. N., Fu, Y., Li, X., Xu, H., *et al.* (2014). Deficiency in LRP6-mediated Wnt signaling contributes to synaptic abnormalities and amyloid pathology in Alzheimer's disease. *Neuron* **84**, 63–77.

Liu, L., Wan, W., Xia, S., Kalionis, B., and Li, Y. (2014). Dysfunctional Wnt/β-catenin signaling contributes to blood-brain barrier breakdown in Alzheimer's disease. *Neurochem. Int.* **75**, 19–25.

Maharzi, N., Parietti, V., Nelson, E., Denti, S., Robledo-Sarmiento, M., Setterblad, N., Parcelier, A., Pla, M., Sigaux, F., Gluckman, J. C., *et al.* (2013). Identification of TMEM131L as a novel regulator of thymocyte proliferation in humans. *J. Immunol.* **190**, 6187–6197.

Malik, B. R., Maddison, D. C., Smith, G. A., and Peters, O. M. (2019). Autophagic and endo-lysosomal dysfunction in neurodegenerative disease. *Mol. Brain* **12**, 100.

Mandler, W. K., Nurkiewicz, T. R., Porter, D. W., Kelley, E. E., and Olfert, I. M. (2018). Microvascular dysfunction following multiwalled carbon nanotube exposure is mediated by thrombospondin-1 receptor CD47. *Toxicol. Sci.* **165**, 90–99.

Mandler, W. K., Nurkiewicz, T. R., Porter, D. W., and Olfert, I. M. (2017). Thrombospondin-1 mediates multi-walled carbon nanotube induced impairment of arteriolar dilation. *Nanotoxicology* **11**, 112–122.

Mannini, B., Vecchi, G., Labrador-Garrido, A., Fabre, B., Fani, G., Franco, J. M., Lilley, K., Pozo, D., Vendruscolo, M., Chiti, F., *et al.* (2019). Differential interactome and innate immune response activation of two structurally distinct misfolded protein oligomers. *ACS Chem. Neurosci.* **10**, 3464–3478.

Mercer, R. R., Scabilloni, J. F., Hubbs, A. F., Wang, L., Battelli, L. A., McKinney, W., Castranova, V., and Porter, D. W. (2013). Extrapulmonary transport of MWCNT following inhalation exposure. *Part. Fibre Toxicol.* **10**, 38.

Miller, M. R., Shaw, C. A., and Langrish, J. P. (2012). From particles to patients: Oxidative stress and the cardiovascular effects of air pollution. *Future Cardiol.* **8**, 577–602.

Mitchell, L. A., Lauer, F. T., Burchiel, S. W., and McDonald, J. D. (2009). Mechanisms for how inhaled multiwalled carbon nanotubes suppress systemic immune function in mice. *Nat. Nanotechnol.* **4**, 451–456.

Mitsuyama, Y., and Koide, T. (2018). Microtubule-associated protein 1 B rescues memory decline in Alzheimer ' s disease model mice. *Ann. Alzheimer's Dement. Care* **2**, 1–6.

Mizuno, E., Kawahata, K., Kato, M., Kitamura, N., and Komada, M. (2003). STAM proteins bind ubiquitinated proteins on the early endosome via the VHS domain and ubiquitin-interacting motif. *Mol. Biol. Cell* **14**, 3675–3689.

Mostovenko, E., Young, T., Muldoon, P. P., Bishop, L., Canal, C. G., Vucetic, A., Zeidler-Erdely, P. C., Erdely, A., Campen, M. J., and Ottens, A. K. (2019). Nanoparticle exposure driven circulating bioactive peptidome causes systemic inflammation and vascular dysfunction. *Part. Fibre Toxicol.* **16**, 20.

Muller, J., Huaux, F., Moreau, N., Misson, P., Heilier, J. F., Delos, M., Arras, M., Fonseca, A., Nagy, J. B., and Lison, D. (2005). Respiratory toxicity of multi-wall carbon nanotubes. *Toxicol. Appl. Pharmacol.* **207**, 221–231.

Nemmar, A., Hoet, P. H. M., Vanquickenborne, B., Dinsdale, D., Thomeer, M., Hoylaerts, M. F., Vanbilloen, H., Mortelmans, L., and Nemery, B. (2002). Passage of inhaled particles into the blood circulation in humans. *Circulation* **105**, 411–414.

Niwa, Y., Hiura, Y., Murayama, T., Yokode, M., and Iwai, N. (2007). Nano-sized carbon black exposure exacerbates atherosclerosis in LDL-receptor knockout mice. *Circ. J.* **71**, 1157–1161.

Nixon, R. A. (2005). Endosome function and dysfunction in Alzheimer's disease and other neurodegenerative diseases. *Neurobiol. Aging* **26**, 373–382. p

Nurkiewicz, T. R., Porter, D. W., Barger, M., Millecchia, L., Rao, K. M. K., Marvar, P. J., Hubbs, A. F., Castranova, V., and Boegehold, M. A. (2006). Systemic microvascular dysfunction and inflammation after pulmonary particulate matter exposure. *Environ. Health Perspect.* **114**, 412–419.

Oppenheim, H. A., Lucero, J. A., Guyot, A. C., Herbert, L. M., McDonald, J. D., Mabondzo, A., and Lund, A. K. (2013). Exposure to vehicle emissions results in altered blood brain barrier permeability and expression of matrix metalloproteinases and tight junction proteins in mice. *Part. Fibre Toxicol.* **10**, 62.

Oren-Suissa, M., Gattegno, T., Kravtsov, V., and Podbilewicz, B. (2017). Extrinsic repair of injured dendrites as a paradigm for regeneration by fusion in *Caenorhabditis elegans*. *Genetics* **206**, 215–230.

Palenzuela, R., Gutiérrez, Y., Draffin, J. E., Lario, A., Benoist, M., and Esteban, J. A. (2017). MAP1B light chain modulates synaptic transmission via AMPA receptor intracellular trapping. *J. Neurosci.* **37**, 9945–9963.

Pardridge, W. M. (2016). CSF, blood-brain barrier, and brain drug delivery. *Expert Opin. Drug Deliv.* **13**, 963–975.

Paul, J., Strickland, S., and Melchor, J. P. (2007). Fibrin deposition accelerates neurovascular damage and neuroinflammation in mouse models of Alzheimer's disease. *J. Exp. Med.* **204**, 1999–2008.

Peng, C., Yan, S., Ye, J., Shen, L., Xu, T., and Tao, W. (2012a). Vps18 deficiency inhibits dendritogenesis in Purkinje cells by blocking the lysosomal degradation of lysyl oxidase. *Biochem. Biophys. Res. Commun.* **423**, 715–720.

Peng, C., Ye, J., Yan, S., Kong, S., Shen, Y., Li, C., Li, Q., Zheng, Y., Deng, K., Xu, T., *et al.* (2012b). Ablation of vacuole protein sorting 18 (Vps18) gene leads to neurodegeneration and impaired neuronal migration by disrupting multiple vesicle transport pathways to lysosomes. *J. Biol. Chem.* **287**, 32861–32873.

Petersen, M. A., Ryu, J. K., Chang, K. J., Etxeberria, A., Bardehle, S., Mendiola, A. S., Kamau-Devers, W., Fancy, S. P. J., Thor, A., Bushong, E. A., *et al.* (2017). Fibrinogen activates BMP signaling in oligodendrocyte progenitor cells and inhibits remyelination after vascular damage. *Neuron* **96**, 1003–1012.e7.

Porter, D. W., Hubbs, A. F., Mercer, R. R., Wu, N., Wolfarth, M. G., Sriram, K., Leonard, S., Battelli, L., Schwegler-Berry, D., and Friend, S. (2010). Mouse pulmonary dose- and time course-responses induced by exposure to multi-walled carbon nanotubes. *Toxicology* **269**, 136–147.

Pous, L., Deshpande, S. S., Nath, S., Mezey, S., Malik, S. C., Schildge, S., Bohrer, C., Topp, K., Pfeifer, D., Fernández-Klett, F., *et al.* (2020). Fibrinogen induces neural stem cell differentiation into astrocytes in the subventricular zone via BMP signaling. *Nat. Commun.* **11**, 630.

Rao, S. K., Ross, J. M., Harrison, F. E., Bernardo, A., Reiserer, R. S., Mobley, J. A., and McDonald, M. P. (2015). Differential proteomic and behavioral effects of long-term voluntary exercise in wild-type and APP-overexpressing transgenics. *Neurobiol. Dis.* **78**, 45–55.

Reddy, A. R., Krishna, D. R., Reddy, Y. N., and Himabindu, V. (2010). Translocation and extra pulmonary toxicities of multi wall carbon nanotubes in rats. *Toxicol. Mech. Methods* **20**, 267–272.

Ryan, N. S., Keihaninejad, S., Shakespeare, T. J., Lehmann, M., Crutch, S. J., Malone, I. B., Thornton, J. S., Mancini, L., Hyare, H., Yousry, T., *et al.* (2013). Magnetic resonance imaging evidence for presymptomatic change in thalamus and caudate in familial Alzheimer's disease. *Brain* **136**, 1399–1414.

Sargent, L. M., Porter, D. W., Staska, L. M., Hubbs, A. F., Lowry, D. T., Battelli, L., Siegrist, K. J., Kashon, M. L., Mercer, R. R., Bauer, A. K., *et al.* (2014). Promotion of lung adenocarcinoma following inhalation exposure to multi-walled carbon nanotubes. *Part. Fibre Toxicol.* **11**, 3.

Schachtrup, C., Ryu, J. K., Helmrick, M. J., Vagena, E., Galanakis, D. K., Degen, J. L., Margolis, R. U., and Akassoglou, K. (2010). Fibrinogen triggers astrocyte scar formation by promoting the availability of active TGF-β after vascular damage. *J. Neurosci.* **30**, 5843–5854.

Schikowski, T., Vossoughi, M., Vierkötter, A., Schulte, T., Teichert, T., Sugiri, D., Fehsel, K., Tzivian, L., Bae, I. S., Ranft, U., *et al.* (2015). Association of air pollution with cognitive functions and its modification by APOE gene variants in elderly women. *Environ. Res.* **142**, 10–16.

Schindelin, J., Arganda-Carreras, I., Frise, E., Kaynig, V., Longair, M., Pietzsch, T., Preibisch, S., Rueden, C., Saalfeld, S., Schmid, B., *et al.* (2012). Fiji: An open-source platform for biological-image analysis. *Nat. Methods* **9**, 676–682.

Schousboe, A., Sickmann, H. M., Bak, L. K., Schousboe, I., Jajo, F. S., Faek, S. A. A., and Waagepetersen, H. S. (2011). Neuron-glia interactions in glutamatergic neurotransmission: Roles of oxidative and glycolytic adenosine triphosphate as energy source. *J. Neurosci. Res.* **89**, 1926–1934.

Selkoe, D. J. (2019). Early network dysfunction in Alzheimer's disease. *Science* **365**, 540–541.

Shimojo, M., Takuwa, H., Takado, Y., Tokunaga, M., Tsukamoto, S., Minatohara, K., Ono, M., Seki, C., Maeda, J., Urushihata, T., *et al.* (2020). Selective disruption of inhibitory synapses leading to neuronal hyperexcitability at an early stage of tau pathogenesis in a mouse model. *J. Neurosci.* **40**, 3491–3501.

Tabet, L., Bussy, C., Amara, N., Setyan, A., Grodet, A., Rossi, M. J., Pairon, J. C., Boczkowski, J., and Lanone, S. (2009). Adverse effects of industrial multiwalled carbon nanotubes on human pulmonary cells. *J. Toxicol. Environ. Health A* **72**, 60–73.

Tortosa, E., Montenegro-Venegas, C., Benoist, M., Härtel, S., González-Billault, C., Esteban, J. A., and Avila, J. (2011). Microtubule-associated protein 1B (MAP1B) is required for dendritic spine development and synaptic maturation. *J. Biol. Chem.* **286**, 40638–40648.

Upadhyay, S., Stoeger, T., Harder, V., Thomas, R. F., Schladweiler, M. C., Semmler-Behnke, M., Takenaka, S., Karg, E., Reitmeir, P., Bader, M., *et al.* (2008). Exposure to ultrafine carbon particles at levels below detectable pulmonary inflammation affects cardiovascular performance in spontaneously hypertensive rats. *Part. Fibre Toxicol.* **5**, 19.

Vecchia, D., and Pietrobon, D. (2012). Migraine: A disorder of brain excitatory-inhibitory balance? *Trends Neurosci.* **35**, 507–520.

Vico Varela, E., Etter, G., and Williams, S. (2019). Excitatory-inhibitory imbalance in Alzheimer's disease and therapeutic significance. *Neurobiol. Dis.* **127**, 605–615.

Walker, V. G., Li, Z., Hulderman, T., Schwegler-Berry, D., Kashon, M. L., and Simeonova, P. P. (2009). Potential in vitro effects of carbon nanotubes on human aortic endothelial cells. *Toxicol. Appl. Pharmacol.* **236**, 319–328.

Wang, Y., Xiong, L., and Tang, M. (2017). Toxicity of inhaled particulate matter on the central nervous system: Neuroinflammation, neuropsychological effects and neurodegenerative disease. *J. Appl. Toxicol.* **37**, 644–667.

Whyte, L. S., Lau, A. A., Hemsley, K. M., Hopwood, J. J., and Sargeant, T. J. (2017). Endo-lysosomal and autophagic dysfunction: A driving factor in Alzheimer's disease? *J. Neurochem.* **140**, 703–717.

Yamada, M., Takeshita, T., Miura, S., Murata, K., Kimura, Y., Ishii, N., Nose, M., Sakagami, H., Kondo, H., Tashiro, F., *et al.* (2001). Loss of hippocampal CA3 pyramidal neurons in mice lacking STAM1. *Mol. Cell. Biol.* **21**, 3807–3819.

Yi, H. A., Möller, C., Dieleman, N., Bouwman, F. H., Barkhof, F., Scheltens, P., Van Der Flier, W. M., and Vrenken, H. (2016). Relation between subcortical grey matter atrophy and conversion from mild cognitive impairment to Alzheimer's disease. *J. Neurol. Neurosurg. Psychiatry* **87**, 425–432.

Zhang, Z., Bai, M., Barbosa, G. O., Chen, A., Wei, Y., Luo, S., Wang, X., Wang, B., Tsukui, T., Li, H., *et al.* (2020). Broadly conserved roles of TMEM131 family proteins in intracellular collagen assembly and secretory cargo trafficking. *Sci. Adv.* **6**, eaay7667.